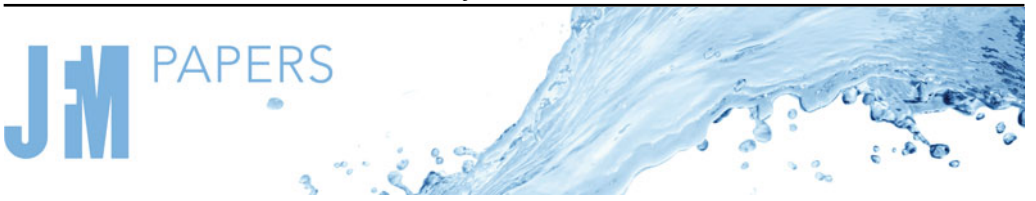
J. Fluid Mech. (2026), *vol.* 1027, A41, doi:10.1017/jfm.2025.11057



Synchronisation in two-dimensional damped-driven Navier–Stokes turbulence: insights from data assimilation and Lyapunov analysis

Masanobu Inubushi[1,2] **and Colm-cille P. Caulfield**[3,4]

[1]Department of Applied Mathematics, Tokyo University of Science, Tokyo 162-8601, Japan

[2]Graduate School of Engineering Science, The University of Osaka, Osaka 560-8531, Japan

[3]Institute for Energy and Environmental Flows, University of Cambridge, Cambridge CB3 0EZ, UK

[4]Department of Applied Mathematics and Theoretical Physics, University of Cambridge, Cambridge CB3 0WA, UK

Corresponding author: Masanobu Inubushi, inubushi@rs.tus.ac.jp

(Received 26 August 2025; revised 4 November 2025; accepted 7 December 2025)

In Navier–Stokes (NS) turbulence, large-scale turbulent flows inevitably determine small-scale flows. Previous studies using data assimilation with the three-dimensional (3-D) NS equations indicate that employing observational data resolved down to a specific length scale, $\ell_*^{3\text{-D}}$, enables the successful reconstruction of small-scale flows. Such a length scale of 'essential resolution of observation' for reconstruction $\ell_*^{3\text{-D}}$ is close to the dissipation scale in three-dimensional NS turbulence. Here, we study the equivalent length scale in two-dimensional (2-D) NS turbulence, $\ell_*^{2\text{-D}}$, and compare with the three-dimensional case. Our numerical studies using data assimilation and conditional Lyapunov exponents reveal that, for Kolmogorov flows with Ekman drag, the length scale $\ell_*^{2\text{-D}}$ is actually close to the forcing scale, substantially larger than the dissipation scale. Furthermore, we discuss the origin of the significant relative difference between the length scales, $\ell_*^{2\text{-D}}$ and $\ell_*^{3\text{-D}}$, based on inter-scale interactions, 'cascades' and orbital instabilities in turbulence dynamics.

Key words: Navier-Stokes equations, nonlinear dynamical systems, turbulent flows

© The Author(s), 2026. Published by Cambridge University Press. This is an Open Access article, distributed under the terms of the Creative Commons Attribution licence (https://creativecommons.org/licenses/by/4.0/), which permits unrestricted re-use, distribution and reproduction, provided the original article is properly cited.

https://doi.org/10.1017/jfm.2025.11057 Published online by Cambridge University Press

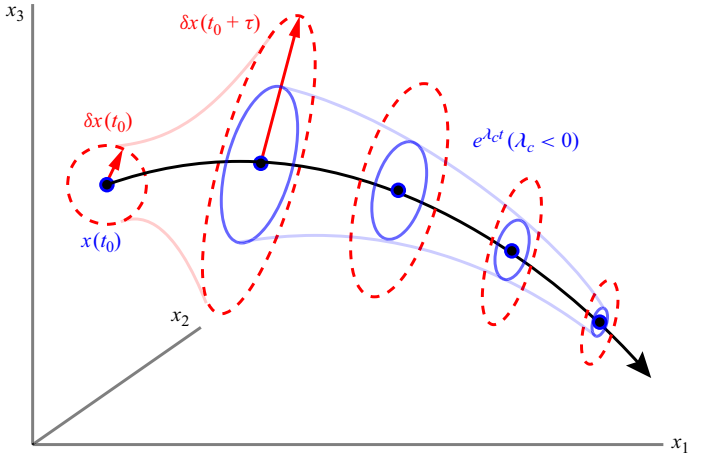


Figure 1. Schematic of orbital instability and data assimilation in a chaotic dynamical system. Orbital instability expands uncertainty (dashed ellipses), whereas data assimilation contracts uncertainty (solid ellipses) along the trajectory. The figure illustrates a case in which data assimilation succeeds, with the uncertainty contracting exponentially along the orbit, characterised by the negative conditional Lyapunov exponent λ_c (< 0), as $e^{\lambda_c t}$.

1. Introduction

Sensitive dependence on initial conditions is one of the crucial properties of turbulence dynamics. Considering turbulence as a chaotic dynamical system, we can characterise it using the (maximum) Lyapunov exponent, which measures the speed of exponential growth of uncertainty in a state space. Let us consider a dynamical system defined by differential equations, $\dot{x} = F(x)$, with some initial condition, $x(t_0) = x_0 \in \mathbb{R}^N$. Precise data on the initial conditions x_0 are not available in practice due to the limitation of measurement and so it is natural to introduce an initial uncertainty around x_0. Schematically, the uncertainty is shown as a red ball in figure 1.

In a chaotic dynamical system, uncertainty grows exponentially fast in the most unstable direction, $\delta x(t_0 + \Delta\tau)$, depicted by a red arrow and ellipsoid in figure 1, and $\|\delta x(t_0 + \Delta\tau)\| \propto \|\delta x(t_0)\| e^{\lambda_1 \Delta\tau}$ where λ_1 (> 0) is the (maximum) Lyapunov exponent. When we consider the mentioned differential equations as the Navier–Stokes (NS) equations, the positive Lyapunov exponent λ_1 indicates the sensitive dependence on initial conditions of turbulence, which makes prediction difficult. Specifically, it is conjectured that for three-dimensional turbulence, the positive Lyapunov exponent is the inverse of the Kolmogorov time $(\nu/\epsilon)^{1/2}$, where ν is the kinematic viscosity and ϵ is the kinetic energy dissipation rate (Ruelle 1979); thus, uncertainty grows with the fastest time scale in turbulence.

What if we could observe the state? Although complete observation of the state would eliminate uncertainty, it is unrealistic in practice. Instead, it is natural to assume that we can observe large-scale structures of turbulence. In other words, we can make partial or incomplete observation, since we can only observe at a relatively low resolution, where the key control parameter is the resolution of our observations. The wavenumber corresponding to the resolution is denoted by k_a, and we assume that data on a low-pass filtered field with $k < k_a$ are available.

If the resolution is too low, i.e. k_a is too small, the chaotic dynamics would still expand the uncertainty along the orbit. However, if we can obtain observational data with sufficiently high resolution, i.e. k_a is sufficiently large, the introduction of observational

https://doi.org/10.1017/jfm.2025.11057 Published online by Cambridge University Press

data overcomes chaotic dynamics and reduces the uncertainty in the state, which is represented by the blue ellipsoid in figure 1. This is an interpretation of data assimilation (DA) from the viewpoint of dynamical systems theory. The outcome of DA, whether successful or not, is determined by the competition between uncertainty expansion by chaotic dynamics and uncertainty reduction through assimilation using observational data. Interestingly, for three-dimensional turbulence in a periodic box, if k_a exceeds a critical value, $k_a \geqslant k_a^{*(3\text{-D})} := 0.2/\eta$, where η is the Kolmogorov length scale, the assimilation process progressively reduces and eventually eliminates the uncertainty. In other words, the small-scale structure associated with $k \geqslant k_a$ converges asymptotically to the true unobserved structure under the DA process. This critical value is less dependent on the details of external forcing and DA algorithms. Since Yoshida, Yamaguchi & Kaneda (2005) first discovered this property through direct numerical simulations in a periodic box, the DA approach has attracted increasing attention and has been extended to various three-dimensional turbulent systems, including wall turbulence (see Zaki 2024 and references therein). Moreover, the synchronisation property of turbulence plays a key role in applications. For example, the above-mentioned critical wavenumber, $k_a^{*(3\text{-D})}$, is associated with the stability transition of machine learning-based turbulence models (Matsumoto, Inubushi & Goto 2024).

The competition inherent in the DA process can be mathematically formulated as a bifurcation problem, specifically referred to as the 'blowout bifurcation' in the context of chaos synchronisation (Inubushi *et al.* 2023). Within this framework, the rate of uncertainty growth or reduction in the DA process can be quantified using the conditional Lyapunov exponent, denoted by λ_c (see figure 1). In particular, the critical wavenumber, k_a^*, can be identified by the sign change of the conditional Lyapunov exponent, which also plays a central role in the present study in analysing the synchronisation.

Turbulence dynamics strongly depends on the spatial dimension. In this paper, we demonstrate that a remarkable distinction between two- and three-dimensional turbulence emerges in their synchronisation properties. Regarding DA in the two-dimensional NS equations, a seminal paper by Olson & Titi (2003) rigorously established a sufficient condition for successful DA, based on the concept of determining modes (Foias *et al.* 2001), and this led to new DA schemes with more general observables. Despite the critical importance of their series of results, they appear to be under-recognised within the turbulence physics community. Here, we revisit this problem with the novel tool of the conditional Lyapunov exponent. In particular, we identify the critical wavenumber in two-dimensional turbulence, $k_a^{*(2\text{-D})}$, compare it with the equivalent critical wavenumber in three-dimensional turbulence, $k_a^{*(3\text{-D})}$, and discuss the underlying key physical differences in the dominant flow dynamics. In § 2, we present the mathematical formulation of the problem and describe the numerical methods. The principal contributions of this study are twofold: the numerical findings for Kolmogorov flow with Ekman drag, presented in § 3; and the physical interpretation of their dimensional dependence, proposed in § 4. Finally, in § 5, we provide concluding remarks and discuss directions for future work.

2. Formulation and methods

Here, we present the mathematical formulation of DA for the NS equations, following Olson & Titi (2003). In addition to single-run DA experiments, we introduce the conditional Lyapunov exponent as a long-time averaged quantity of the equations, based on Inubushi *et al.* (2023).

https://doi.org/10.1017/jfm.2025.11057 Published online by Cambridge University Press

2.1. *Continuous data assimilation of the Navier–Stokes equations*

Two-dimensional turbulence is significant not only in mathematical physics but also as a basis for understanding (for example) atmospheric and oceanic flows. In particular, we focus on Kolmogorov flows as an extremely simplified model. However, two-dimensional NS flows driven by a forcing term consisting of a single eigenmode of the Laplacian, including Kolmogorov flows, cannot sustain turbulence with a broad energy spectrum (Constantin, Foias & Manley 1994). Here, we introduce Ekman drag, which is a natural physical mechanism to prevent energy accumulation in low-wavenumber regions (Boffetta & Ecke 2012). Kolmogorov flow with Ekman drag has also been widely used as a benchmark test in machine learning applications (for example, Shankar *et al.* 2025). Therefore, a precise understanding of the dynamics of this system is crucial across various fields of fluid mechanics.

Kolmogorov flow with Ekman drag is described by the NS equations with an incompressible velocity field,

$$\frac{\partial \boldsymbol{u}}{\partial t} + \boldsymbol{u}\cdot\nabla\boldsymbol{u} = -\nabla\pi + \nu\Delta\boldsymbol{u} - \alpha\boldsymbol{u} + \boldsymbol{f}, \quad \nabla\cdot\boldsymbol{u} = 0, \tag{2.1}$$

where $\boldsymbol{u}(\boldsymbol{x}, t)$ and $\pi(\boldsymbol{x}, t)$ is the velocity and pressure field on a two-dimensional torus $\mathbb{T}^2 = [0, 2\pi]^2$, i.e. $\boldsymbol{u} : \mathbb{T}^2 \times [0, \infty] \to \mathbb{R}^2$ and $\pi : \mathbb{T}^2 \times [0, \infty] \to \mathbb{R}$. The external forcing is of so-called Kolmogorov type, $\boldsymbol{f} = \sin(k_f y)\boldsymbol{e}_x$, ν and α are the kinematic viscosity and the friction coefficient of the Ekman drag, respectively. As was done by Olson & Titi (2003), the spatial mean of $\boldsymbol{u}$ over $\mathbb{T}^2$, i.e. the mean flow, is set to zero.

We introduce the projections P_{k_a} and Q_{k_a} in the Fourier representation as a mathematical model of incomplete observation, which is defined by

$$P_{k_a}\boldsymbol{u} = \sum_{|\boldsymbol{k}|<k_a} \hat{\boldsymbol{u}}_{\boldsymbol{k}} e^{i\boldsymbol{k}\cdot\boldsymbol{x}} \quad \text{and} \quad Q_{k_a} = I - P_{k_a}, \tag{2.2}$$

where $\hat{\boldsymbol{u}}_{\boldsymbol{k}}$ is the Fourier coefficient of the velocity field $\boldsymbol{u}$ for the wavenumber $\boldsymbol{k} \in \mathbb{Z}^2$. This defines the observation of large-scale structures discussed in § 1. We assume that the low-pass filtered field is observable, i.e. $\boldsymbol{p} := P_{k_a}\boldsymbol{u}$, while the unobserved small-scale velocity field corresponds to $\boldsymbol{q} := Q_{k_a}\boldsymbol{u}$. Note that the key parameter k_a controls the resolution of the observation as it defines the orthogonal decomposition of the velocity fields into the large-scale and small-scale structures, $\boldsymbol{u} = \boldsymbol{p} + \boldsymbol{q}$. For notational simplicity, we hereafter denote (2.1) by

$$\frac{\partial \boldsymbol{u}}{\partial t} = \boldsymbol{N}(\boldsymbol{p}, \boldsymbol{q}), \tag{2.3}$$

and, by using the decomposition, the evolution equations for the large-scale structures field $\boldsymbol{p}$ and the small-scale structures field $\boldsymbol{q}$ are

$$\frac{\partial \boldsymbol{p}}{\partial t} = P_{k_a}\boldsymbol{N}(\boldsymbol{p}, \boldsymbol{q}) =: \boldsymbol{F}(\boldsymbol{p}, \boldsymbol{q}) \quad \text{and} \quad \frac{\partial \boldsymbol{q}}{\partial t} = Q_{k_a}\boldsymbol{N}(\boldsymbol{p}, \boldsymbol{q}) =: \boldsymbol{G}(\boldsymbol{p}, \boldsymbol{q}). \tag{2.4}$$

The goal is to infer the unobserved small-scale field $\{\boldsymbol{q}(t)\}_{t\geqslant 0}$ from the observational data of $\{\boldsymbol{p}(t)\}_{t\geqslant 0}$. To this end, we employ the method of continuous data assimilation (CDA). We introduce an approximation velocity field, $\tilde{\boldsymbol{u}}$, which is decomposed as $\tilde{\boldsymbol{u}} = \tilde{\boldsymbol{p}} + \tilde{\boldsymbol{q}}$ in the same way as $\boldsymbol{u}$. In the CDA process, using the observational data, we set $\tilde{\boldsymbol{p}}(t) \equiv \boldsymbol{p}(t)$ for $\forall t \geqslant 0$, a process called direct insertion, and then solve the relevant equations for the approximate small-scale structures field within the CDA framework:

https://doi.org/10.1017/jfm.2025.11057 Published online by Cambridge University Press

$$\frac{\partial \tilde{\boldsymbol{q}}}{\partial t} = \boldsymbol{G}(\boldsymbol{p}, \tilde{\boldsymbol{q}}) \tag{2.5}$$

with some initial values $\tilde{\boldsymbol{q}}(0) = \tilde{\boldsymbol{q}}_0$. We expect that if k_a is sufficiently large, using the CDA process, the approximation velocity field will converge to the actual velocity field or, equivalently,

$$\tilde{\boldsymbol{q}}(t) \to \boldsymbol{q}(t) \quad (t \to +\infty) \tag{2.6}$$

from an arbitrary initial value, as confirmed in three-dimensional turbulence (Zaki 2024). In such a case, we say that the small-scale flow $\boldsymbol{q}(t)$ is synchronised or slaved to the large-scale flow $\boldsymbol{p}(t)$, since the sequential data of $\{\boldsymbol{p}(t)\}_{t\geqslant 0}$ uniquely determine the asymptotic state of $\{\boldsymbol{q}(t)\}_{t\geqslant 0}$ after the transient period.

2.2. *Conditional Lyapunov exponent*

The notion of uncertainty is formulated geometrically by a perturbation vector to the velocity field, i.e. $\boldsymbol{u} + \delta\boldsymbol{u}$, where $\delta\boldsymbol{u}$ represents an error in measurement. Let us consider the decomposition of the perturbation as $\delta\boldsymbol{u} = \delta\boldsymbol{p} + \delta\boldsymbol{q}$, as before. In the CDA framework, we assume that there is no uncertainty in large-scale flows, as it is directly observable. This assumption is mathematically equivalent to the condition $\delta\boldsymbol{p}(t) \equiv \boldsymbol{0}$ for $\forall t \geqslant 0$. Therefore, the uncertainty exists only in small-scale flows, i.e. $\boldsymbol{q} + \delta\boldsymbol{q}$. In a case where the CDA process has been successful, formulated by the condition (2.6), the synchronised state, i.e. the true small-scale structure field $\boldsymbol{q}$, is expected to be asymptotically stable. Hence, if we write $\tilde{\boldsymbol{q}} = \boldsymbol{q} + \delta\boldsymbol{q}$, the condition (2.6) is equivalent to $\delta\boldsymbol{q}(t) \to \boldsymbol{0}$ $(t \to +\infty)$ for an arbitrary initial perturbation vector field, $\delta\boldsymbol{q}(0) = \delta\boldsymbol{q}_0$.

To perform linear stability analysis, we further assume that the perturbation is infinitesimally small. From the relation $\tilde{\boldsymbol{q}} = \boldsymbol{q} + \delta\boldsymbol{q}$, with the evolution equations of $\boldsymbol{q}$ in (2.4), the linearisation of the (2.5) results in

$$\frac{\partial \delta\boldsymbol{q}}{\partial t} = D_{\boldsymbol{q}}\boldsymbol{G}(\boldsymbol{p}, \boldsymbol{q})\delta\boldsymbol{q}, \tag{2.7}$$

where $D_{\boldsymbol{q}}\boldsymbol{G}$ is the Fréchet derivative and $(\boldsymbol{p}(t), \boldsymbol{q}(t))$ is the solution of the Navier–Stokes equation (2.3) on the turbulence attractor. If the norm of the perturbation decays, $\|\delta\boldsymbol{q}(t)\| \to 0$ $(t \to +\infty)$, the uncertainty vanishes, which means that the CDA has been successful. Exponential convergence is characterised by the conditional Lyapunov exponent (CLE),

$$\lambda_c := \lim_{T\to+\infty} \frac{1}{T} \ln \frac{\|\delta\boldsymbol{q}(T)\|}{\|\delta\boldsymbol{q}(0)\|} \tag{2.8}$$

if the limit exists. It is an ergodic quantity that characterises the turbulence attractor of the NS equations. In particular, it does not depend on any specific DA algorithm or the initial conditions. A negative CLE indicates convergence of the CDA process independently of the initial point on the attractor, in contrast to the outcome of a single DA experiment, which may depend on the initial condition.

From its definition, it is clear that the CLE, λ_c, depends on the assimilation wavenumber k_a, which specifies the decomposition of $\boldsymbol{p}$ and $\boldsymbol{q}$. To make this dependence explicit, we denote it by $\lambda_c(k_a)$. The CLE for the case of $k_a = 1$ coincides with the maximum Lyapunov exponent, i.e. $\lambda_c(k_a = 1) = \lambda_1$, as discussed by Inubushi *et al.* (2023). This is because, for $k_a = 1$, we have $\boldsymbol{p} = P_{k_a=1}\boldsymbol{u} = \hat{\boldsymbol{u}}_{\boldsymbol{0}}$ from the definition (2.2). Since we consider flows with zero mean, the Fourier coefficient of the zero mode vanishes; hence, $\hat{\boldsymbol{u}}_{\boldsymbol{0}} = \boldsymbol{0}$. Consequently, the case of $k_a = 1$ corresponds to the situation without observational data, where $\boldsymbol{p} = \boldsymbol{0}$

https://doi.org/10.1017/jfm.2025.11057 Published online by Cambridge University Press

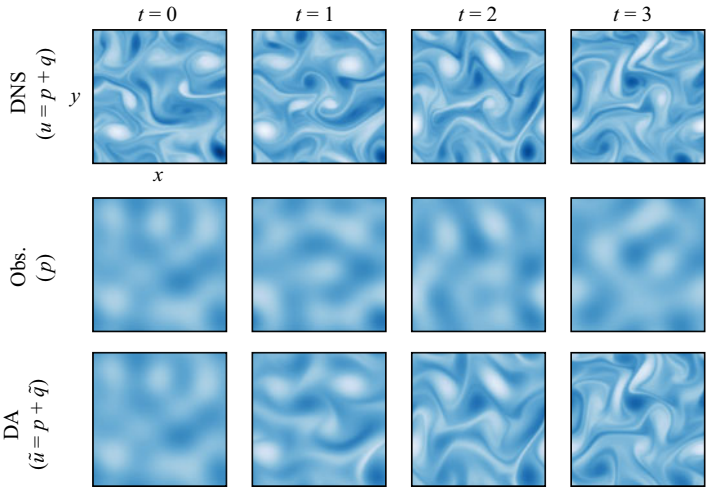


Figure 2. Data assimilation experiment for two-dimensional Navier–Stokes turbulence. Snapshots of vorticity fields at times $t = 0, 1, 2$ and 3, from top to bottom: the reference DNS field $\boldsymbol{u}(t) = \boldsymbol{p}(t) + \boldsymbol{q}(t)$; the observational data $\boldsymbol{p}(t)$ obtained by low-pass filtering the DNS field with $k_a = 4$; and the field obtained through data assimilation (CDA) $\tilde{\boldsymbol{u}}(t) = \boldsymbol{p}(t) + \tilde{\boldsymbol{q}}(t)$. A corresponding video is available as supplementary movie 1 available at https://doi.org/10.1017/jfm.2025.11057.

and $\boldsymbol{u} = \boldsymbol{q}$. In this case, no condition is imposed on the perturbation vector and, thus, the CLE reduces to the maximum Lyapunov exponent, $\lambda_c(k_a = 1) = \lambda_1$.

2.3. *Numerical methods*

The direct numerical simulations are performed using a Fourier spectral method with 128×128 grid points, with dealiasing implemented via the 3/2 rule. Time integration is carried out using a fourth-order Runge–Kutta scheme. In the next section, we first present the results for the case with forcing wavenumber $k_f = 4$, viscosity $\nu = 1.0 \times 10^{-3}$ and linear drag coefficient $\alpha = 1.0 \times 10^{-1}$, as the reference case, followed by an investigation of the dependence of the results on these parameters.

3. Results

Figure 2 presents the results of simulations implementing the CDA process, showing snapshots of the vorticity field, $\omega = \partial_x v - \partial_y u$. The top row, labelled 'DNS', shows the results from direct numerical simulation (DNS) of (2.1), that is, $\boldsymbol{u}(t) = (u(t),\ v(t))^T = \boldsymbol{p}(t) + \boldsymbol{q}(t)$ for $0 \leqslant t \leqslant 3$, taken after the flow has reached a statistically steady state. We also present the results of a simulation implementing the CDA process with $k_a = 4$, initiated at $t = 0$. The middle row of figure 2, labelled 'Obs.', represents the vorticity field of the observation, $\boldsymbol{p}(t)$, obtained by applying a low-pass filter to the DNS data.

The bottom row of figure 2, labelled 'DA', represents the vorticity field constructed from the approximate velocity fields via $\tilde{\omega} = \partial_x \tilde{v} - \partial_y \tilde{u}$, where $\tilde{\boldsymbol{u}}(t) = \boldsymbol{p}(t) + \tilde{\boldsymbol{q}}(t)$ are the results of the simulations implementing the CDA process. The approximate small-scale structure field $\tilde{\boldsymbol{q}}(t)$ is computed by numerically solving (2.5) with the initial condition of $\tilde{\boldsymbol{q}}(0) = \tilde{\boldsymbol{q}}_0 = 0$, with $\boldsymbol{p}(t)$ determined from the DNS results. At the onset of the CDA process, $t = 0$, only a single snapshot of the observation is available and so $\tilde{\boldsymbol{u}}(0) = \boldsymbol{p}(0)$. However, the simulation implementing the CDA process, using successive observational data $\boldsymbol{p}(t)$, gradually reconstructs the unobserved field $\boldsymbol{q}(t)$, suggesting that

https://doi.org/10.1017/jfm.2025.11057 Published online by Cambridge University Press

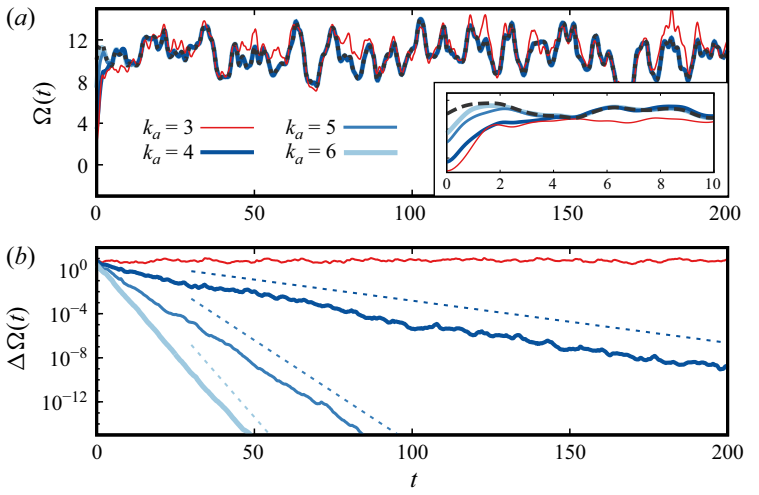


Figure 3. Time series of (*a*) enstrophy $\Omega(t)$, with a close-up view for $0 \leqslant t \leqslant 10$ (inset), and (*b*) the enstrophy-norm error $\Delta\Omega(t)$ as defined in (3.1). The dashed lines show the convergence rates given by the conditional Lyapunov exponents $\lambda_c(k_a)$.

$\tilde{\boldsymbol{q}}(t) \to \boldsymbol{q}(t)$ $(t \to +\infty)$. In particular, at $t = 3$, the filamentary structures in the reconstructed vorticity field corresponding to $\tilde{\boldsymbol{u}}(t)$ closely resemble those in the DNS field, $\boldsymbol{u}(t)$.

Figure 3 shows a time series of enstrophy, $\Omega(t) = (1/2)\|\omega(t)\|_2^2$. The dashed line corresponds to the DNS result, while the solid lines represent the enstrophy of the CDA reconstructions (i.e. $(1/2)\|\tilde{\omega}(t)\|_2^2$). The figure shows the results for wavenumbers $k_a = 3, 4, 5, 6$ (with $k_a = 4$ corresponding to the case shown in figure 2). When the resolution is low, particularly for $k_a = 3$, the enstrophy shows a clear deviation from the DNS result; however, for $k_a \geqslant 4$, the CDA enstrophy converges towards the true value. To examine this convergence in detail, we define the approximation error as

$$\Delta\Omega(t) = \frac{1}{2}\|\omega(t) - \tilde{\omega}(t)\|_2^2, \tag{3.1}$$

and plot this error in figure 3(*b*) using the same line colour as in figure 3(*a*) (the case $k_a = 4$ again corresponds to figure 2). For $k_a \geqslant 4$, the approximation error decays exponentially so $\Delta\Omega(t) \to 0 \quad (t \to \infty)$.

To characterise these simulation results in terms of the ergodic property of the NS equations, we compute the conditional Lyapunov exponent λ_c using variational equation (2.7) for each k_a. The dashed lines in figure 3(*b*) show the exponential decay $\propto e^{2\lambda_c(k_a)t}$. The line slopes are in excellent agreement with the average decay rate of the approximation error $\Delta\Omega(t)$. In particular, we obtain $\lambda_c(k_a) < 0$ for $k_a \geqslant 4$, while $\lambda_c(k_a) > 0$ for $k_a \leqslant 3$. Although specific properties, such as the convergence behaviour of the simulations implementing the CDA process, depend on the initial state $\boldsymbol{u}(0)$ on the turbulence attractor and the initial guess of $\tilde{\boldsymbol{q}}(0)$, the conditional Lyapunov exponent does not. Thanks to this property, we can conclude that, for Kolmogorov flow with $k_f = 4$ studied here, the critical wavenumber $k_a^{*(2\text{-D})}$ for synchronisation satisfies $3 < k_a^{*(2\text{-D})} < 4$. In particular, the critical wavenumber is close to the forcing wavenumber; that is, $k_a^{*(2\text{-D})} \simeq O(k_f)$.

Figure 4 shows the same time series as in figure 3, but in terms of the palinstrophy, i.e. panel (*a*) shows $P(t) = (1/2)\|\nabla\omega(t)\|_2^2$, and panel (*b*) shows $\Delta P(t) = (1/2)\|\nabla(\omega(t) - \tilde{\omega}(t))\|_2^2$. While the palinstrophy is more suitable for characterising small scales in 2-D

https://doi.org/10.1017/jfm.2025.11057 Published online by Cambridge University Press

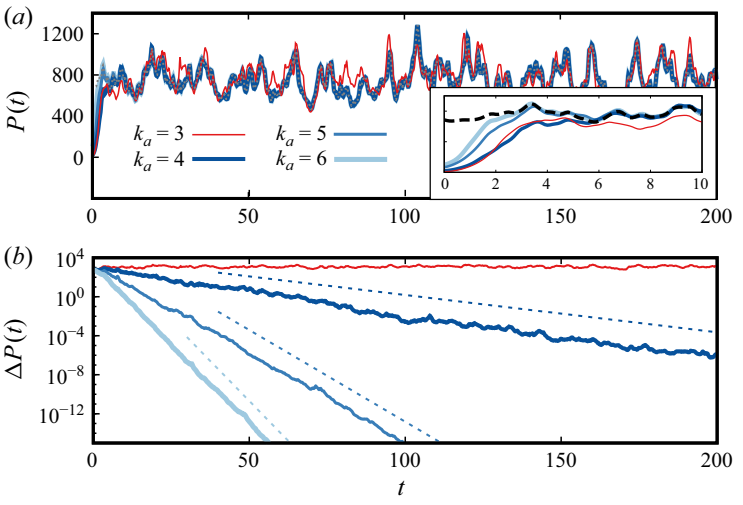


Figure 4. Same as figure 3, with the vertical axis showing the palinstrophy, $P(t)$, and the palinstrophy-norm error, $\Delta P(t)$.

turbulence, the results are essentially the same as those obtained in terms of the enstrophy, since all norms are equivalent in the finite-dimensional system, including the Galerkin-truncated system studied here.

Figure 5 shows the energy spectrum illustrating the synchronisation process across scales. The grey dashed line represents the time-averaged energy spectrum $\langle E(k)\rangle_T$ computed from the DNS data. A power law region can be identified, whose slope is steeper than the slope of the so-called Batchelor–Kraichnan–Leith scaling $E(k) \propto k^{-3}$, due to the effect of the Ekman drag (Boffetta & Musacchio 2017; Valadão *et al.* 2025). As a reference, the straight grey solid line in figure 5 shows the slope of k^{-4} with these axes. The solid lines in figure 5 represent the temporal evolution in the energy spectrum $\Delta E(k, t)$ of the difference of the fields, $\boldsymbol{u}(t) - \tilde{\boldsymbol{u}}(t)$, where $\tilde{\boldsymbol{u}}(t)$ denotes the velocity field obtained from the CDA with $k_a = 4$. The spectrum $\Delta E(k, t)$ represents the distribution of the synchronisation error, in terms of both amplitude and phase, across the scales. With increasing thickness, the lines correspond to the results of $\Delta E(k, t)$ at times $t = 0,\ 10,\ 50,\ 100,\ 150$ and 200. This case is the same as that shown in figure 2, where $\tilde{\boldsymbol{q}}_0 = 0$ at $t = 0$. Therefore, $\tilde{\boldsymbol{q}}(t) \simeq 0$ in the initial period of the CDA process and $\Delta E(k, t) \simeq \langle E(k)\rangle_T$ $(k/k_a \geqslant 1)$. By definition, $\Delta E(k, t) \equiv 0$ for all $k/k_f = k/k_a < 1$ and $t \geqslant 0$, since we assume that the 'ground-truth' DNS data are available for this spectral range and hence no error exists there. As expected from the results shown in figure 2–4, $\Delta E(k, t)$ decreases with time for fixed k.

Interestingly, while decaying in magnitude, the shape of the energy spectrum appears to be preserved. Taking into account the exponential decay characterised by the conditional Lyapunov exponent λ_c, we assume that the energy spectrum evolves in time as $\Delta E(k,\ t) \propto \mathcal{E}(k)e^{-2\lambda_c t}$ with some time-invariant function $\mathcal{E}$. In fact, the scaled energy spectra, $\Delta E(k,\ t)e^{2\lambda_c t}$, do not change their shape for $t \geqslant 100$, as shown in the inset, which suggests the existence of such a time-invariant function $\mathcal{E}(k)$. Introducing observational data reduces the error, $\Delta E(k,\ t)$ for $k \geqslant k_a$ almost uniformly across all scales, which may be related to the non-locality of inter-scale interactions discussed later.

Heretofore, we have fixed the forcing wavenumber at $k_f = 4$, with the parameters viscosity $\nu = 1.0 \times 10^{-3}$ and linear drag coefficient $\alpha = 1.0 \times 10^{-1}$. As a final test,

https://doi.org/10.1017/jfm.2025.11057 Published online by Cambridge University Press

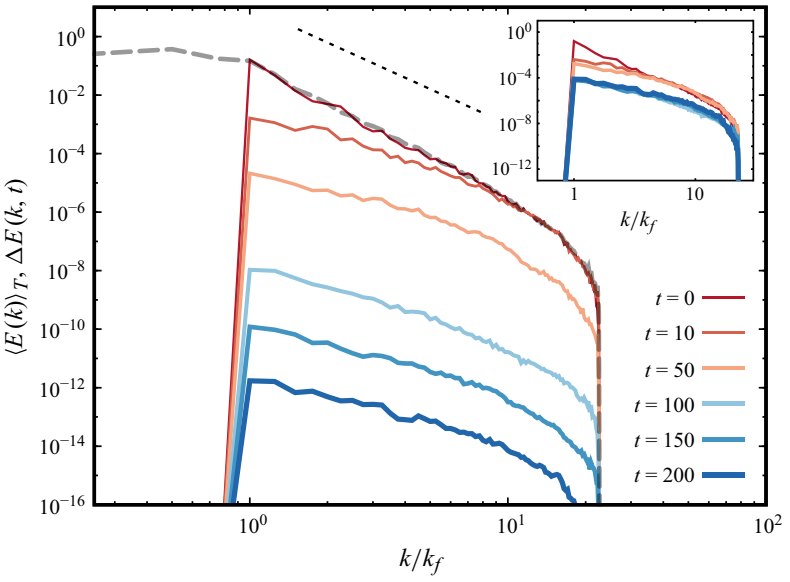


Figure 5. Synchronisation process examined over scales. The solid lines show the time evolution of the energy spectrum of the difference of the fields $\Delta E(k,\ t)$ obtained through the CDA process for the case $k_a = 4$. From thickest to thinnest, the curves correspond to times $t = 0,\ 10,\ 50,\ 100,\ 150$ and 200. The dashed line shows the result of the DNS, corresponding to the long-time-averaged energy spectrum $\langle E(k)\rangle_T$. The inset shows the scaled energy spectra, $\Delta E(k,\ t)e^{2\lambda_c t}$, plotted with the same colours.

we investigate the dependence of the synchronisation properties on the particular choice of k_f, ν and α. Figure 6 shows the conditional Lyapunov exponent as a function of k_a with different forcing wavenumbers $k_f = 2,\ 3,\ \cdots,\ 6$. We exclude the case of $k_f = 1$, for which chaotic dynamics is not observed. The conditional Lyapunov exponent for the case of $k_a = 1$ coincides with the maximum Lyapunov exponent, as discussed in § 2.2, and is positive for all values of k_f, i.e. $\lambda_c(k_a = 1) = \lambda_1 > 0$. With increasing k_a, the observational data reduce uncertainty, so that the conditional Lyapunov exponents decrease monotonically and eventually change sign around each k_f, i.e. $k_a^{*(2\text{-D})} = O(k_f)$.

For larger values of k_a, the asymptotic behaviour of the perturbation $\delta\boldsymbol{q}(t)$ is governed essentially by the viscous and frictional terms, $\partial_t\delta\boldsymbol{q} \simeq -\nu\Delta\delta\boldsymbol{q} - \alpha\delta\boldsymbol{q}$. Consequently, the conditional Lyapunov exponents decrease following $\lambda_c(k_a) \simeq -\nu k_a^2 - \alpha$, which is represented by the dashed curve shown in figure 6. The data of $\lambda_c(k_a)$ for large k_a lie on the curve $-\nu k_a^2 - \alpha$, as observed in three-dimensional turbulence by Inubushi *et al.* (2023). Note that, while the conditional Lyapunov exponents shown in figure 6 are calculated from the long-time average as defined by (2.8), the finite-time dynamics of the perturbation $\delta\boldsymbol{q}(t)$ are not necessarily governed solely by such viscous and frictional effects. Further details of the perturbation dynamics will be reported elsewhere.

The inset of figure 6 shows the same conditional Lyapunov exponents normalised by the time scale associated with the enstrophy injection, τ_I, and the forcing wavenumber, k_f. Following Valadão *et al.* (2025), we define $\tau_I = \eta_I^{-1/3}$, where η_I denotes the enstrophy injection rate, given by $\eta_I := -k_f\langle\overline{\omega\cos(k_f y)}\rangle_T$ for the Kolmogorov-type forcing. Here, the overline denotes the spatial mean. For statistically steady turbulence, the enstrophy injection rate is balanced by the total enstrophy dissipation rate, i.e. $\eta_I = \eta_\nu + \eta_\alpha$ (Boffetta & Ecke 2012), where $\eta_\nu = 2\nu\langle P\rangle_T$ is the dissipation due to viscosity and $\eta_\alpha = 2\alpha\langle\Omega\rangle_T$ is that due to Ekman friction. Valadão *et al.* (2025) identified τ_I as a key

https://doi.org/10.1017/jfm.2025.11057 Published online by Cambridge University Press

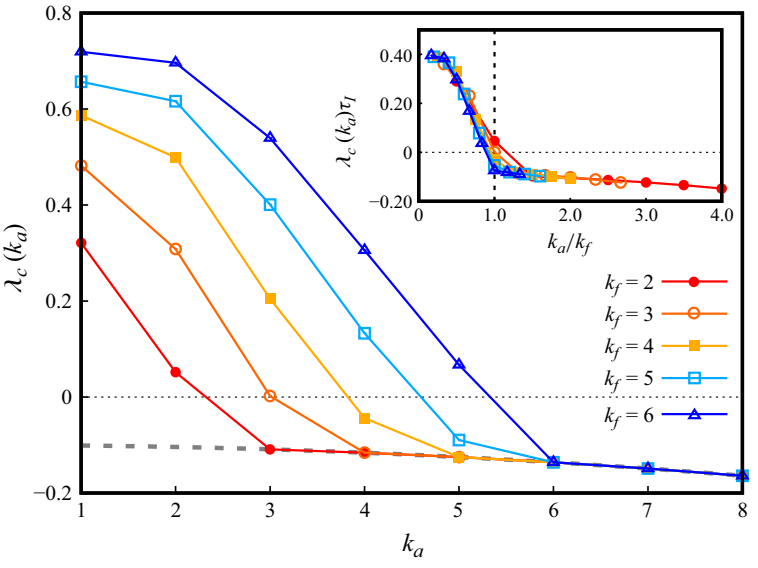


Figure 6. Conditional Lyapunov exponent $\lambda_c(k_a)$ as a function of k_a, for the fixed parameters $\nu = 1.0 \times 10^{-3}$ and $\alpha = 1.0 \times 10^{-1}$, and for different forcing wavenumbers $k_f = 2, 3, \ldots, 6$, represented by filled red circles, open orange circles, yellow filled squares, open light-blue squares and blue triangles, respectively. The grey dashed curve represents $-\nu k_a^2 - \alpha$. The inset shows the same exponents $\lambda_c(k_a)$ normalised by time scale associated with the enstrophy injection τ_I and the forcing wavenumber k_f.

characteristic time scale of two-dimensional Ekman–Navier–Stokes turbulence. The data shown in the inset of figure 6 almost collapse onto a single curve, suggesting the scaling with τ_I and k_f is appropriate. Figures 7 and 8 show the results of the same computation as figure 6, but with different parameter sets, $(\nu, \alpha) = (1.0 \times 10^{-3},\ 5.0 \times 10^{-2})$ and $(\nu, \alpha) = (5.0 \times 10^{-4},\ 1.0 \times 10^{-1})$, respectively. The overall behaviour remains largely unchanged.

The insets of figures 6–8 indicate that $\lambda_c(k_a = 1)\tau_I = \lambda_1 \tau_I \simeq 0.40$ for the maximum Lyapunov exponents. This value is close to 0.42 ± 0.01, which is the maximum Lyapunov exponents normalised by the enstrophy dissipation rate reported by Clark, Tarra & Berera (2020) (see their figure 3). Although their system differs from the present one, for example, because they employed hypoviscosity instead of Ekman drag, this similarity may still be worth noting.

4. Discussion: dimensional dependence of synchronisation properties

The results presented in the previous section strongly suggest that in two-dimensional turbulence as examined here, the critical wavenumber, the lower bound on the resolution of observational data required for data assimilation, coincides with the forcing scale, i.e. $k_a^{*(2\text{-D})} = O(k_f)$. In other words, in two-dimensional turbulence with a forward enstrophy cascade, the number of degrees of freedom associated with the large-scale structures governing the whole dynamics is substantially smaller than the total number of degrees of freedom.

Notably, the critical wavenumber $k_a^{*(2\text{-D})}$ is located at the upper edge of the power-law scaling range. Interestingly, in three-dimensional turbulence in a periodic box, the equivalent critical wavenumber $k_a^{*(3\text{-D})} \simeq 0.2\eta^{-1}$ differs markedly from that in

https://doi.org/10.1017/jfm.2025.11057 Published online by Cambridge University Press

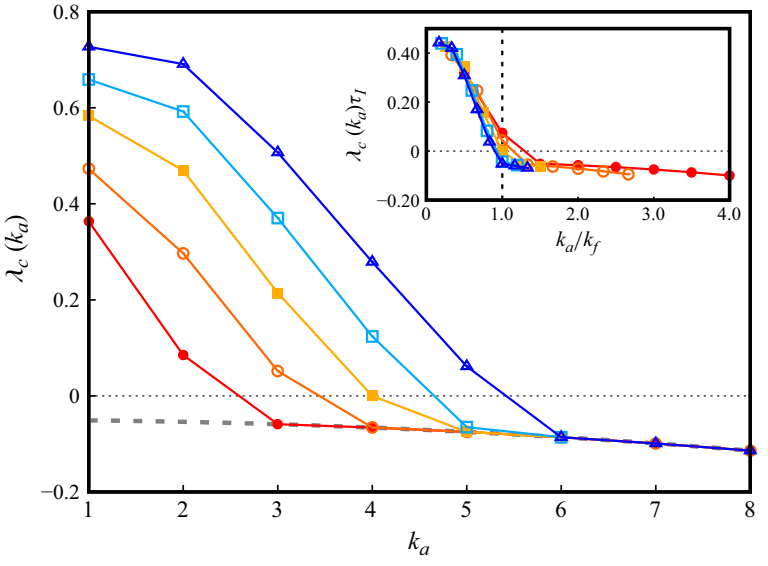


Figure 7. Same as figure 6, for the fixed parameters $(\nu,\,\alpha) = (1.0\times10^{-3},\ 5.0\times10^{-2})$.

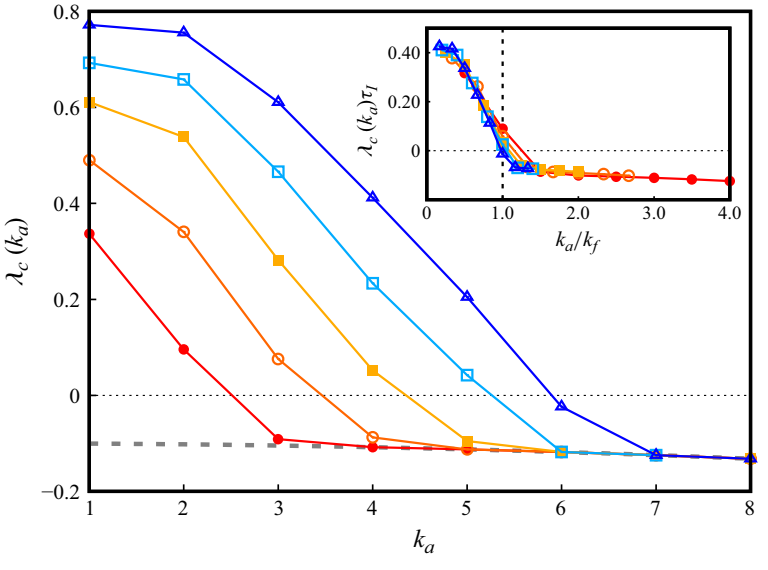


Figure 8. Same as figure 6, for the fixed parameters $(\nu,\,\alpha) = (5.0\times10^{-4},\ 1.0\times10^{-1})$.

the two-dimensional turbulence discussed previously. The critical wavenumber $k_a^{*(3\text{-D})}$ actually lies near the lower edge of the inertial range, i.e. close to the Kolmogorov length scale, and clearly exhibits a dependence on the viscosity ν. As turbulence develops further, achieving synchronisation necessitates increasingly well-resolved observational data in 3-D, but not apparently in 2-D.

To account for the observed dimensional differences in this synchronisation property of NS turbulence, we propose the following physical interpretation. We begin by interpreting the fact that $k_a^{*(3\text{-D})} \simeq 0.2\eta^{-1}$ in three-dimensional turbulence. Specifically, we consider

https://doi.org/10.1017/jfm.2025.11057 Published online by Cambridge University Press

why synchronisation fails when $k_a \ll k_a^{*(3\text{-D})}$; for instance, in a setting where the observational data are restricted to the energy-containing range. In three-dimensional turbulence, interscale interactions are known to be scale-local. Turbulent structures at a given scale predominantly generate smaller-scale structures, specifically, those at approximately 0.58 times the original scale (Yoneda, Goto & Tsuruhashi 2022), which then successively generate smaller and smaller scale structures. Turbulence flow structures are thus generated (at least on average) sequentially from large to small scales, the physical manifestation of the (forward) energy cascade of three-dimensional turbulence. Taking this into consideration, it may be expected that continuously providing observational data at the largest scales would induce the successive formation of smaller-scale structures. The information contained in the observational data is 'transmitted' progressively to smaller scales.

Crucially however, that transmission inevitably involves amplification of uncertainty when $k_a \ll k_a^{*(3\text{-D})}$, as data assimilation fails to reconstruct small-scale structures quantitatively accurately. A key mechanism underlying this failure is the inherent orbital instability of three-dimensional turbulence. As noted in § 1, the maximum Lyapunov exponent of three-dimensional turbulence corresponds to the inverse of the Kolmogorov time scale, capturing the physical phenomenon that the fastest time scales in turbulence inevitably introduce uncertainty. The most unstable spatial mode that amplifies small errors, the Lyapunov vector associated with the maximum Lyapunov exponent, λ_1, exhibits a peak in Fourier space at $k \simeq 0.2\eta^{-1}$ in the energy spectrum (Boffetta & Musacchio 2017; Budanur & Kantz 2022). Furthermore, a study based on the GOY shell model (Yamada & Ohkitani 1988) suggests that the peaks of the less unstable modes, associated with the subsequent positive Lyapunov exponents, $\lambda_i > 0$ $(i \geqslant 2)$, occur at wavenumbers lower than that of the most unstable mode. Hence, all unstable modes associated with the positive Lyapunov exponents exist only at wavenumbers below $0.2\eta^{-1}$. Combining this with the previously described picture of the energy cascade, when $k_a \ll k_a^{*(3\text{-D})}$, while the observational information of large scales is transmitted towards smaller scales in the DA process, the unstable spatial modes amplify small-scale errors exponentially. The 'inverse cascade' of errors (Boffetta & Musacchio 2017) towards larger scales inevitably disrupts the transmitted information and, therefore, the data assimilation fails when $k_a < k_a^{*(3\text{-D})}$. However, when the observational data include all unstable modes, i.e. $k_a > k_a^{*(3\text{-D})}$, there now exists no mechanism by which errors can be amplified and so data assimilation is successful.

In the case of two-dimensional turbulence, the physical mechanism underlying the critical wavenumber $k_a^{*(2\text{-D})} = O(k_f)$ is qualitatively different, although perhaps not as clear as in the three-dimensional case. The properties of two-dimensional turbulence can strongly depend on the details of the forcing and the energy dissipation mechanism (Boffetta & Ecke 2012), and few studies have examined its orbital instability. Consequently, understanding the origin of the critical wavenumber through this particular lens is challenging. Nevertheless, it is reasonable to expect that the non-locality of inter-scale interactions (Ohkitani 1990) and the orbital instability play key roles in two-dimensional flows. Non-local inter-scale interactions dominate in two-dimensional turbulence, and indeed it is well known that there is an inverse energy cascade in two-dimensional turbulence (Boffetta & Ecke 2012), at least suggestive of the fact that larger scale structures 'know' about smaller scale structures that are 'pumping' energy up-scale. As a result, even when observational data are available only in the energy-containing range (i.e. $k_a = O(k_f)$), information can be transmitted across scales via

https://doi.org/10.1017/jfm.2025.11057 Published online by Cambridge University Press

non-local interactions, making it possible to reconstruct directly small-scale structures. It appears, at least heuristically, that the required small-scale structures to cascade energy upscale to form (and maintain) the observed larger scale structures emerge (and survive) spontaneously in a way that remains consistent with the downscale enstrophy cascade. Furthermore, Yamada & Ohkitani (1988) suggests that all unstable modes associated with the positive Lyapunov exponents in two-dimensional turbulence exist only at wavenumbers below $O(k_f)$. Therefore, when the observational data include all unstable modes, i.e. $k_a \geqslant O(k_f)$, there exists no mechanism for error amplification and small-scale structures are directly reconstructed via the non-local inter-scale interactions (again consistently with the inverse energy cascade and the forward enstrophy cascade); that is, data assimilation can be successful.

5. Conclusion

Synchronisation in turbulence is a key property to understand turbulence dynamics and has been studied extensively for three-dimensional turbulence. The present study initiates a new direction of research into two-dimensional turbulence by introducing a novel approach based on synchronisation. Specifically, through the use of the data assimilation method and Lyapunov analysis, we have demonstrated that the essential resolution of observations for flow field reconstruction in forced two-dimensional turbulence is surprisingly lower than the equivalent essential resolution in forced three-dimensional turbulence. More precisely, in the two-dimensional turbulent flows studied here, the critical wavenumber for reconstruction is close to the forcing scale, i.e. $k_a^{*(\text{2-D})} = O(k_f)$, while the critical wavenumber for the equivalent three-dimensional turbulent flows is close to the dissipation scale, i.e. $k_a^{*(\text{3-D})} \simeq 0.2/\eta$. We further propose physical mechanisms underlying the difference in synchronisation properties, based on the (non-)locality of interscale interactions and orbital instabilities in turbulence dynamics.

Compared with three-dimensional turbulence, the understanding of synchronisation properties from the perspective of turbulence physics remains somewhat more speculative in two-dimensional flows, despite their importance. Also, while we have identified the critical wavenumber $k_a^{*(\text{2-D})}$ for two-dimensional Kolmogorov flows with Ekman drag, establishing the generality of this result through extensions of the present work remains an important challenge for future research. Only recently have the fundamental properties of Ekman–Navier–Stokes turbulence, namely the correction to the energy spectrum, been clarified using GPU-based computations over a wide range of parameters of ν and α (Valadão *et al.* 2025). Although the calculation of the conditional Lyapunov exponents λ_c requires a considerable additional computational cost beyond that of the DNS, extending the present analysis to a broader parameter range will be an important next step. In particular, clarifying the relationship between the time scale associated with synchronisation, characterised by λ_c, and the relevant time scales within turbulence will provide valuable insight into the fundamental understanding of turbulence.

Beyond this, it is crucial to study further the synchronisation properties of two-dimensional turbulence with, for example, a more detailed consideration of the inverse energy cascade and realistic boundary conditions. In particular, studying synchronisation in two-dimensional turbulence that exhibits a double cascade (Boffetta & Ecke 2012) is intriguing. In three-dimensional turbulence, Clark Di Leoni, Mazzino & Biferale (2020) identified the critical wavenumber $k_a^{*(\text{3-D})} \simeq 0.2/\eta$ as the characteristic scale where the nonlinear and viscous energy fluxes are in balance. A complementary approach combining such flux-based and Lyapunov analyses is crucial for elucidating the dynamics of

https://doi.org/10.1017/jfm.2025.11057 Published online by Cambridge University Press

two-dimensional turbulence. Furthermore, it would be particularly interesting to consider flows with other physical mechanisms such as rotation and stratification that can lead, at least in some regimes, to quasi-two-dimensional dynamics, providing a natural test-bed to investigate transitions from behaviour associated with the two 'pure' end members of exactly two-dimensional and inherently three-dimensional flows. In this context, it will be valuable to summarise systematically the critical wavenumbers associated with synchronisation during such transitions from two- to three-dimensional systems, using the framework developed in this study. Finally, it is also essential to develop a quantitative framework that solidifies the interpretation presented in the previous section, where quantifying information transmission across scales in turbulent dynamics, as explored by, for example, Tanogami & Araki (2024, 2025), will play a crucial role. Pursuing this direction could offer valuable insight into the fundamental nature of turbulence.

Supplementary movie. Supplementary movie is available at https://doi.org/10.1017/jfm.2025.11057. The upper part of the video corresponds to the vorticity fields shown in figure 2(*a*) (from left to right: the velocity field obtained from DNS, $\boldsymbol{u}(t) = \boldsymbol{p}(t) + \boldsymbol{q}(t)$; the observational data $\boldsymbol{p}(t)$; and the data assimilation result $\tilde{\boldsymbol{u}}(t) = \boldsymbol{p}(t) + \tilde{\boldsymbol{q}}(t)$). The lower part displays the corresponding enstrophy. In particular, the blue solid line indicates the enstrophy $\Omega(t)$ of the DNS solution, the blue dashed line represents the approximate enstrophy arising from the simulation implementing the CDA process, and the red solid line shows the enstrophy error denoted $\Delta\Omega(t)$ and defined in (3.1).

Acknowledgements. The authors are grateful to the three anonymous reviewers whose detailed and constructive comments helped improve the focus and overall quality of the manuscript. M.I. gratefully acknowledges M. Yamada and E. S. Titi for their insightful discussions, and the hospitality of the Department of Applied Mathematics and Theoretical Physics at the Centre for Mathematical Sciences, University of Cambridge, where this work was carried out during his sabbatical leave. Part of the direct numerical simulations of the Navier–Stokes equations was conducted using the supercomputer systems at the Japan Aerospace Exploration Agency (JAXA-JSS2).

Funding. This work was partially supported by JSPS Grants-in-Aid for Scientific Research (Grants No. 24H00186, No. 22K03420 and No. 22H05198).

Declaration of interests. The authors report no conflict of interest.

Data availability statement. The data that support the findings of this study are available from the corresponding author upon reasonable request.

References

Boffetta, G. & Ecke, R.E. 2012 Two-dimensional turbulence. *Annu. Rev. Fluid Mech.* **44**, 427–451.

Boffetta, G. & Musacchio, S. 2017 Chaos and predictability of homogeneous-isotropic turbulence. *Phys. Rev. Lett.* **119**, 054102.

Budanur, N.B. & Kantz, H. 2022 Scale-dependent error growth in Navier–Stokes simulations. *Phys. Rev. E* **106**, 045102.

Clark Di Leoni, P., Mazzino, A. & Biferale, L. 2020 Synchronization to big data: nudging the Navier–Stokes equations for data assimilation of turbulent flows. *Phys. Rev. X* **10** (1), 011023.

Clark, D., Tarra, L. & Berera, A. 2020 Chaos and information in two-dimensional turbulence. *Phys. Rev. Fluids* **5**, 064608.

Constantin, P., Foias, C. & Manley, O.P. 1994 Effects of the forcing function spectrum on the energy spectrum in 2-D turbulence. *Phys. Fluids* **6**, 427–429.

Foias, C., Manley, O., Rosa, R. & Temam, R. 2001 *Navier–Stokes Equations and Turbulence*. Cambridge University Press.

Inubushi, M., Saiki, Y., Kobayashi, M.U. & Goto, S. 2023 Characterizing small-scale dynamics of Navier–Stokes turbulence with transverse Lyapunov exponents: a data assimilation approach. *Phys. Rev. Lett.* **131**, 254001.

Matsumoto, S., Inubushi, M. & Goto, S. 2024 Stable reproducibility of turbulence dynamics by machine learning. *Phys. Rev. Fluids* **9**, 104601.

Ohkitani, K. 1990 Nonlocality in a forced two-dimensional turbulence. *Phys. Fluids A* **2**, 1529–1531.

https://doi.org/10.1017/jfm.2025.11057 Published online by Cambridge University Press

OLSON, E. & TITI, E.S. 2003 Determining modes for continuous data assimilation in 2D turbulence. *J. Stat. Phys.* **113**, 799–840.

RUELLE, D. 1979 Microscopic fluctuations and turbulence. *Phys. Lett. A* **72**, 81–82.

SHANKAR, V., CHAKRABORTY, D., VISWANATHAN, V. & MAULIK, R. 2025 Differentiable turbulence: closure as a partial differential equation constrained optimization. *Phys. Rev. Fluids* **10**, 024605.

TANOGAMI, T. & ARAKI, R. 2024 Information-thermodynamic bound on information flow in turbulent cascade. *Phys. Rev. Res.* **6**, 013090.

TANOGAMI, T. & ARAKI, R. 2025 Scale-to-scale information flow amplifies turbulent fluctuations. *Phys. Rev. Res.* **7**, 023078.

VALADÃO, V.J., BOFFETTA, G., DE LILLO, F., MUSACCHIO, S. & CRIALESI-ESPOSITO, M. 2025 Spectrum correction in Ekman–Navier–Stokes turbulence. *J. Turbul.* **26**, 143–152.

YAMADA, M. & OHKITANI, K. 1988 The inertial subrange and non-positive Lyapunov exponents in fully-developed turbulence. *Prog. Theor. Phys.* **79**, 1265–1268.

YONEDA, T., GOTO, S. & TSURUHASHI, T. 2022 Mathematical reformulation of the Kolmogorov–Richardson energy cascade in terms of vortex stretching. *Nonlinearity* **35**, 1380–1401.

YOSHIDA, K., YAMAGUCHI, J. & KANEDA, Y. 2005 Regeneration of small eddies by data assimilation in turbulence. *Phys. Rev. Lett.* **94**, 014501.

ZAKI, T.A. 2024 Turbulence from an observer perspective. *Annu. Rev. Fluid Mech.* **57**, 311–334.

https://doi.org/10.1017/jfm.2025.11057 Published online by Cambridge University Press